



Tidally Excited Inertial Waves in Stars and Planets: Exploring the Frequency-dependent and Averaged Dissipation with Nonlinear Simulations

Aurélie Astoul and Adrian J. Barker

School of Mathematics, University of Leeds, Leeds LS2 9JT, UK

Received 2023 June 2; revised 2023 August 18; accepted 2023 August 28; published 2023 September 22

Abstract

We simulate the nonlinear hydrodynamical evolution of tidally excited inertial waves in convective envelopes of rotating stars and giant planets modeled as spherical shells containing incompressible, viscous, and adiabatically stratified fluid. This model is relevant for studying tidal interactions between close-in planets and their stars, as well as close low-mass star binaries. We explore in detail the frequency-dependent tidal dissipation rates obtained from an extensive suite of numerical simulations, which we compare with linear theory, including with the widely employed frequency-averaged formalism to represent inertial wave dissipation. We demonstrate that the frequency-averaged predictions appear to be quite robust and are approximately reproduced in our nonlinear simulations spanning the frequency range of inertial waves as we vary the convective envelope thickness, tidal amplitude, and Ekman number. Yet, we find nonlinear simulations can produce significant differences with linear theory for a given tidal frequency (potentially by orders of magnitude), largely due to tidal generation of differential rotation and its effects on the waves. Since the dissipation in a given system can be very different both in linear and nonlinear simulations, the frequency-averaged formalism should be used with caution. Despite its robustness, it is also unclear how accurately it represents tidal evolution in real (frequency-dependent) systems.

Unified Astronomy Thesaurus concepts: [Tidal interaction \(1699\)](#); [Tidal friction \(1698\)](#); [Astrophysical fluid dynamics \(101\)](#); [Hydrodynamics \(1963\)](#); [Star-planet interactions \(2177\)](#); [Exoplanet dynamics \(490\)](#); [Exoplanet tides \(497\)](#); [Close binary stars \(254\)](#); [Low mass stars \(2050\)](#); [Hot Jupiters \(753\)](#); [Extrasolar gaseous planets \(2172\)](#); [Hydrodynamical simulations \(767\)](#)

1. Introduction

Tidal interactions play an important role in driving spin-orbit evolution in planetary and close stellar binary systems (e.g., Zahn 2013; Ogilvie 2014). A key mechanism in low-mass stars and giant planets with convective envelopes is tidal excitation of inertial waves (hereafter IWs) if the perturbed body rotates sufficiently rapidly. IWs are essentially incompressible disturbances in rotating fluids restored by Coriolis forces, which propagate in approximately neutrally stratified convection zones. These waves are excited by tidal forcing if the tidal frequency ω satisfies $|\omega| \leq 2\Omega$, where Ω is the rotational angular velocity. The properties of these waves, and their contribution to tidal dissipation (hence to tidal torques and spin-orbit evolution), depend strongly on the internal structure of the body (varying with stellar mass, age, rotation, and metallicity; Mathis 2015; Bolmont et al. 2017; Gallet et al. 2017; Barker 2020) and physical mechanisms at play (such as differential rotation or magnetism; Baruteau & Rieutord 2013; Guenel et al. 2016; Lin & Ogilvie 2018; Wei 2018; Astoul et al. 2019).

Most prior work studying tidal IWs has employed linear theory of a nonmagnetized viscous fluid in a uniformly rotating spherical shell (e.g., Ogilvie & Lin 2004, 2007; Goodman & Lackner 2009; Ogilvie 2009; Rieutord & Valdettaro 2010). Linear theory is valid if tidal amplitudes are sufficiently small for nonlinearities to be unimportant. However, some close-in planets (such as Hot Jupiters) and stars in close binary systems

may have sufficiently large tidal amplitudes for important nonlinear effects that could considerably alter tidal dissipation rates. We have therefore started to explore in detail the nonlinear evolution of tidally excited IWs in convective envelopes of stars and giant planets in Astoul & Barker (2022; hereafter AB22), building upon Favier et al. (2014) and Barker (2016).

For astrophysical modeling of tidal spin-orbit evolution in planetary and stellar systems, many authors have employed the linear frequency-averaged IW dissipation following Ogilvie (2013). This is obtained by applying an impulsive tidal forcing to obtain an ordinary differential equation describing the wave-like response of the fluid, which can be straightforwardly solved to determine the frequency-averaged IW dissipation. For a piece-wise homogeneous stellar model, this provides simple analytical expressions for tidal dissipation rates and quality factors due to IWs, as employed in many prior studies (e.g., Mathis 2015; Bolmont & Mathis 2016; Gallet et al. 2017; Barker 2020; and many others). More recently, this has been computed using realistic stellar models (Barker 2020, not piece-wise homogeneous), applied to model planetary orbital migration (Lazovik 2021), and to explain the circularization of solar-type stellar binaries (Barker 2022). Despite its simplicity and wide usage to model stellar and planetary populations, the robustness of frequency-averaged dissipation predictions from linear theory has yet to be verified in nonlinear simulations, or those incorporating turbulent convection, differential rotation, or magnetic fields (though a magnetized homogeneous shell in linear theory has been studied by Lin & Ogilvie 2018 and Wei 2018).

We build upon AB22 and model nonlinear tidally forced IWs in neutrally stratified spherical shells in three dimensions,



Original content from this work may be used under the terms of the [Creative Commons Attribution 4.0 licence](#). Any further distribution of this work must maintain attribution to the author(s) and the title of the work, journal citation and DOI.

representing convective envelopes of low-mass stars (from M to F spectral types, with masses ranging from 0.4 to $1.4M_{\odot}$) or giant gaseous planets. We explore the parameter space covering the entire range of wave frequencies for IWs (between -2Ω and $+2\Omega$ in the fluid frame), radial aspect ratios α (ratio of inner to outer radii, i.e., shell thickness, to model various stars and planets), and Ekman numbers E (ratio of viscous to Coriolis forces), so as to determine the validity of linear theoretical predictions, including the frequency-averaged dissipation measure commonly applied to model astrophysical systems. We introduce our model in Section 2, discuss our results in Section 3, present applications to observed astrophysical systems in Section 4, and finally, conclude in Section 5.

2. Modeling Nonlinear Tidal Inertial Waves

We adopt the model of AB22 to study tidally forced IWs with frequency ω , in an adiabatically stratified, incompressible, viscous fluid, in a spherical shell with constant density ρ and initial uniform rotation Ω . In the frame rotating at the rate $\Omega = \Omega \mathbf{e}_z$ of the tidally perturbed body (with spherical coordinates (r, θ, φ)), the wavelike response, with velocity field \mathbf{u} and pressure p , satisfies the momentum and continuity equations (AB22):

$$\begin{aligned} \partial_t \mathbf{u} + (\mathbf{u} \cdot \nabla) \mathbf{u} + 2\Omega \wedge \mathbf{u} &= -\frac{\nabla p}{\rho} + \mathbf{f}_t + \nu \Delta \mathbf{u}, \\ \nabla \cdot \mathbf{u} &= 0. \end{aligned} \quad (1)$$

Here $\mathbf{f}_t = -2\Omega \wedge \mathbf{u}_e$ is the Coriolis acceleration on the nonwavelike tidal flow \mathbf{u}_e (equivalent to the conventional equilibrium tide here), which acts as an effective body force to excite (inertial) wavelike tides (e.g., Ogilvie 2013). The volume-integrated tidal dissipation rate is $D_\nu = -\langle \rho \mathbf{u} \cdot \Delta \mathbf{u} \rangle$ (where $\langle \cdot \rangle$ denotes a volume integral), with ν assumed to be a constant effective viscosity modeling the action of convection on wavelike tides. This assumption is motivated in particular by Duguid et al. (2020, and references therein) and Vidal & Barker (2020a, 2020b) albeit for equilibrium tides, though the treatment of convective effects in this way is still debated (Terquem 2021; Barker & Astoul 2021). The time-averaged D_ν balances the corresponding tidal power $P_t = \langle \mathbf{u} \cdot \mathbf{f}_t \rangle$ in a steady state.

We adopt the planetary/stellar radius R , and Ω^{-1} , as our units of length and time, respectively. The nonwavelike tidal flow \mathbf{u}_e is described by a set of time-dependent equations in linear theory¹: the momentum, continuity, and Poisson equations, and leading-order quasi-hydrostatic equilibrium (plus boundary conditions of a tidally perturbed free surface at $r=R$ and impenetrability on $r=\alpha R$; Ogilvie 2013). We consider only the tidal component with a harmonic degree and order $l=m=2$ (using spherical harmonics Y_l^m), which is (one of) the dominant component(s) for asynchronous (eccentricity) tides in a coplanar two-body system, so

$$\mathbf{u}_e = \text{Re} [i\omega \nabla X(r, \theta, \varphi) e^{-i\omega t}], \quad (2)$$

with

$$X(r, \theta, \varphi) = \frac{C_t}{2(1-\alpha^5)} \left[r^2 + \frac{2}{3} \alpha^5 r^{-3} \right] Y_2^2(\theta, \varphi), \quad (3)$$

where $C_t = (1 + \text{Re}[k_2^2])\epsilon$ is the tidal forcing amplitude, related to the real part of the quadrupolar Love number $\text{Re}[k_2^2]$ (subsequently abbreviated to k_2) and the tidal amplitude parameter $\epsilon = (M_2/M_1)(R/a)^3$ (M_2 and M_1 are masses of the perturber and perturbed body, respectively, the latter has radius R and orbital semimajor axis a).

We introduce several quantities to analyze our simulations. The energy in the differential rotation E_{dr} , triggered by nonlinear IW interactions, integrated over the volume V of the shell, is defined as (see also Tilgner 2007; Favier et al. 2014; Astoul & Barker 2022)

$$E_{dr} = \frac{\rho}{2} \langle [(\mathbf{u}_\varphi)_\varphi - \delta\Omega r \sin\theta]^2 \rangle, \quad (4)$$

where $\langle \cdot \rangle_\varphi$ denotes a φ -average, and

$$\delta\Omega = \frac{1}{V} \left\langle \frac{u_\varphi}{r \sin\theta} \right\rangle \quad (5)$$

is the mean rotation rate of the fluid in the Ω -frame, where $\Omega^* = \Omega + \delta\Omega$ is the modified rotation rate in the inertial frame.² The zonal flow strength depends on the tidal forcing amplitude C_t , and different scaling laws can be derived for low and high C_t (as done in Appendix A.1).

For modeling tidal evolution, we wish to compute the dissipation rate (or tidal power). A useful quantity is the modified tidal quality factor Q' , which is proportional to the ratio between the maximum stored tidal energy and the time-averaged dissipation rate (Goldreich 1963). To obtain this from simulations we compute the dimensionless tidal dissipation rate D_ν , related to the imaginary part of the Love number $\text{Im}[k_2^2]$ according to Ogilvie (2013) and Lin & Ogilvie (2018):

$$\hat{D}_\nu(\omega) = \frac{5R\Omega}{8\pi G} |A|^2 \omega \text{Im}[k_2^2(\omega)], \quad (6)$$

where $\hat{D}_\nu(\omega) = \rho\Omega^3 R^5 D_\nu(\omega)$ is the dimensional tidal dissipation rate, A is the tidal potential amplitude proportional to $GM_2 R^2/a^3 = \epsilon\omega_d^2 R^2$, and $\omega_d = \sqrt{GM_1/R^3}$ is the characteristic dynamical frequency. This leads to

$$|\text{Im}[k_2^2(\omega)]| = \frac{6}{5} \frac{\epsilon_t^2}{C_t^2} \frac{D_\nu(\omega)}{|\omega|}, \quad (7)$$

and hence the frequency-dependent modified tidal quality factor (for $l=m=2$):

$$Q' \equiv \frac{3}{2|\text{Im}[k_2^2(\omega)]|} = \frac{5}{4} \frac{C_t^2}{\epsilon_t^2} \frac{|\omega|}{D_\nu(\omega)}, \quad (8)$$

where $\epsilon_t = \epsilon_\Omega(1+k_2)$, and $\epsilon_\Omega = \Omega/\omega_d$ is small when the body is slowly rotating (which justifies neglecting centrifugal forces). The frequency-averaged $\text{Im}[k_2^2]$ is defined as

$$\Lambda \equiv \int_{-\infty}^{+\infty} \text{Im}[k_2^2(\omega)] \frac{d\omega}{\omega}, \quad (9)$$

¹ But it is perfectly maintained on the timescale of our simulations, meant to be short compared with tidal evolution timescales (see also Appendix A.2).

² $\delta\Omega$ is nonzero not from tidal synchronization—we do not observe this gradual process directly since we study short snapshots in the evolution of the system—but because of the induced differential rotation.

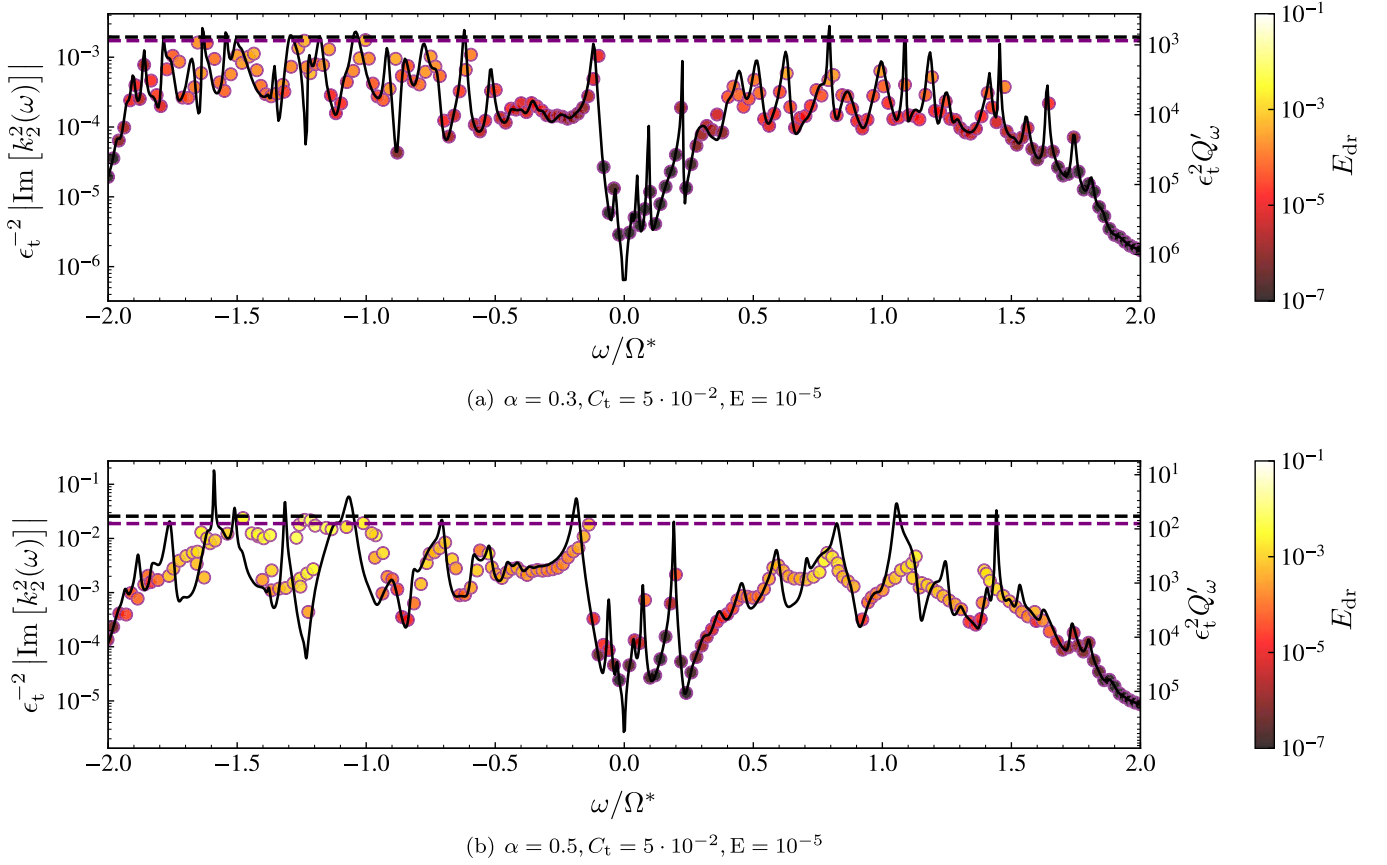


Figure 1. Tidal dissipation from simulations as a function of frequency in the fluid frame ω/Ω^* . We show the rescaled imaginary part of the Love number $\epsilon_t^{-2} |\text{Im}[k_2^2(\omega)]|$ (left y-axis) and the tidal quality factor $\epsilon_t^2 Q'_\omega$ (right y-axis). Colors represent energy in the differential rotation E_{dr} . The black solid and dashed lines show the frequency-dependent and frequency-averaged linear predictions given by Equations (7) and (10), respectively, while the purple dashed line is the frequency-averaged nonlinear tidal dissipation from Equation (9). Top: radial aspect ratio $\alpha = 0.3$ and tidal forcing amplitude $C_t = 5 \cdot 10^{-2}$. E_{dr} is maximal when $\omega = -1.24$ with $E_{dr} \approx 6.2 \cdot 10^{-4}$, and minimal when $\omega = 0.12$ with $E_{dr} \approx 4.6 \cdot 10^{-10}$. Bottom: the same for a thicker envelope with $\alpha = 0.5$. E_{dr} is maximal when $\omega = -1.16$ with $E_{dr} \approx 9.5 \cdot 10^{-3}$, and minimal when $\omega = 2.0$ with $E_{dr} = 1.7 \cdot 10^{-8}$.

with corresponding tidal quality factor $Q' = 3/(2\Lambda)$.

In an incompressible fluid body containing a rigid core, Ogilvie (2013) derived a simple expression for the frequency-averaged tidal dissipation³:

$$\Lambda = \frac{16\pi}{63} \frac{\alpha^5}{1 - \alpha^5} \epsilon_t^2. \quad (10)$$

Since the value of ϵ_t is specific to a given stellar/planetary system and is usually not well-known, we rescale Equations (7)–(10) to remove it in Figures 1, 2, and 4.

3. Nonlinear Tidal Dissipation: Results

We solve Equation (1) with the 3D pseudo-spectral code MagIC⁴ (version 5.10), adopting stress-free impenetrable conditions on spherical boundaries at $r = \alpha R$ and $r = R$. We mostly fix the Ekman number $E = \nu/(\Omega R^2)$ to 10^{-5} unless otherwise stated, and we vary $\omega \in [-2\Omega, 2\Omega]$ for different C_t and radial aspect ratios $\alpha \in \{0.3, 0.5, 0.7, 0.9\}$. The frequency range is scanned using 200 equally spaced values for each α

and C_t (and E), which is a fair compromise between having a sufficiently good coverage of the frequency spectrum to obtain a robust frequency-averaged dissipation,⁵ but with a reasonable total computational cost. In most simulations, we set the maximum spherical harmonic degree to $l_{\max} = 85$ (256 longitudinal and 128 latitudinal grid points, respectively) and use $n_r = 97$ radial (Chebyshev) grid points, though higher radial and horizontal resolutions are used when necessary to ensure convergence. In some simulations we used $n_\varphi = 512$ ($l_{\max} = 170$) to guarantee adequate horizontal resolution (at least 3 orders of magnitude difference in the energy spectrum between the peak and the highest resolvable wavenumbers). Simulations are usually run for times $t \gtrsim 5000 \Omega^{-1}$, which is usually sufficient to reach an averaged steady state. We use a CNAB2 scheme with an adaptive timestep satisfying a Courant–Friedrichs–Lewy condition no larger than $dt = 10^{-2} \Omega^{-1}$ to guarantee adequate time resolution.

We start our investigation with a thick convective envelope ($\alpha = 0.3$) relevant to model main-sequence M-type stars with masses $\sim 0.35 M_\odot$ (e.g., Amard et al. 2016; Gallet et al. 2017), and giant planets possessing solid or stably stratified fluid cores. This also models young low-mass stars with $M \gtrsim 0.4 M_\odot$

³ Equation (10) is equivalent to Equation (113) in Ogilvie (2013) without assuming the same core and envelope density.

⁴ <https://magic-sph.github.io/>

⁵ With this frequency spacing, the error upon integrating to obtain the frequency-averaged value is a few percent in linear calculations. The discrepancy is harder to quantify in nonlinear simulations since we do not know the true value a priori, and exploring this is a primary aim.

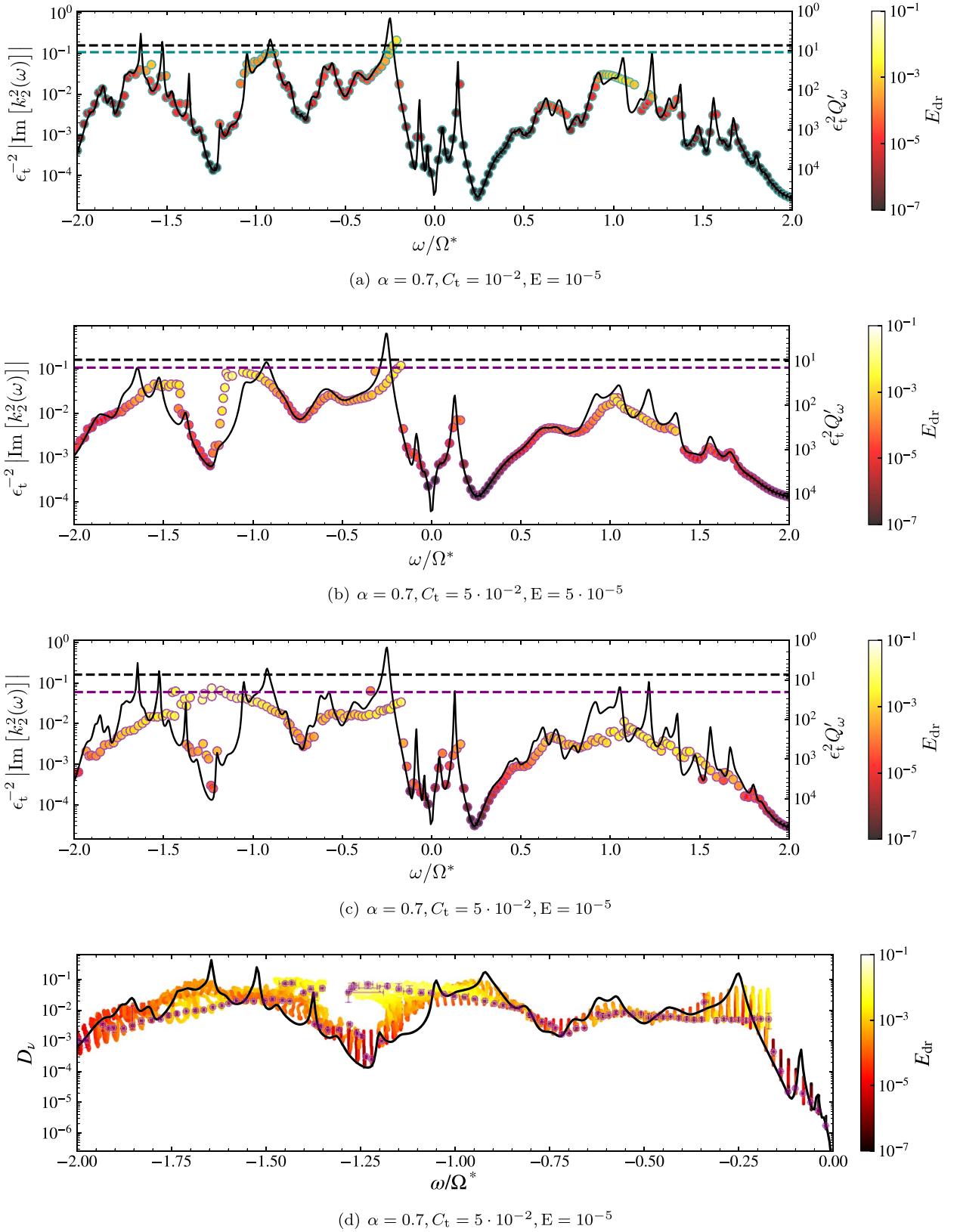


Figure 2. The same as Figure 1 but for a solar-like convective envelope with $\alpha = 0.7$. (a) $C_t = 10^{-2}$. Differential rotation is maximal when $\omega = -0.22$ with $E_{dr} = 1.6 \cdot 10^{-3}$, and minimal when $\omega = 0.24$ with $E_{dr} = 7.0 \cdot 10^{-11}$. (b) $C_t = 5 \cdot 10^{-2}$ and $E = 5 \cdot 10^{-5}$. Differential rotation is maximal when $\omega = -1.06$ with $E_{dr} = 1.2 \cdot 10^{-2}$, and minimal when $\omega = 0.26$ with $E_{dr} = 2.8 \cdot 10^{-8}$. (c) $C_t = 5 \cdot 10^{-2}$ (and $E = 10^{-5}$ again). E_{dr} is maximal when $\omega = -1.14$ with $E_{dr} = 3.1 \cdot 10^{-2}$, and minimal when $\omega = 0.24$ with $E_{dr} = 4.1 \cdot 10^{-8}$. D_ν can differ by up to 3 orders of magnitude at a given frequency depending on E_{dr} . (d) The same as (c) but colored curves instead show the evolution of D_ν and ω/Ω^* during each simulation until (in most cases) an averaged steady state is reached. Error bars indicate variations in the last $2000\Omega^{-1}$ compared to the final value (purple dots).

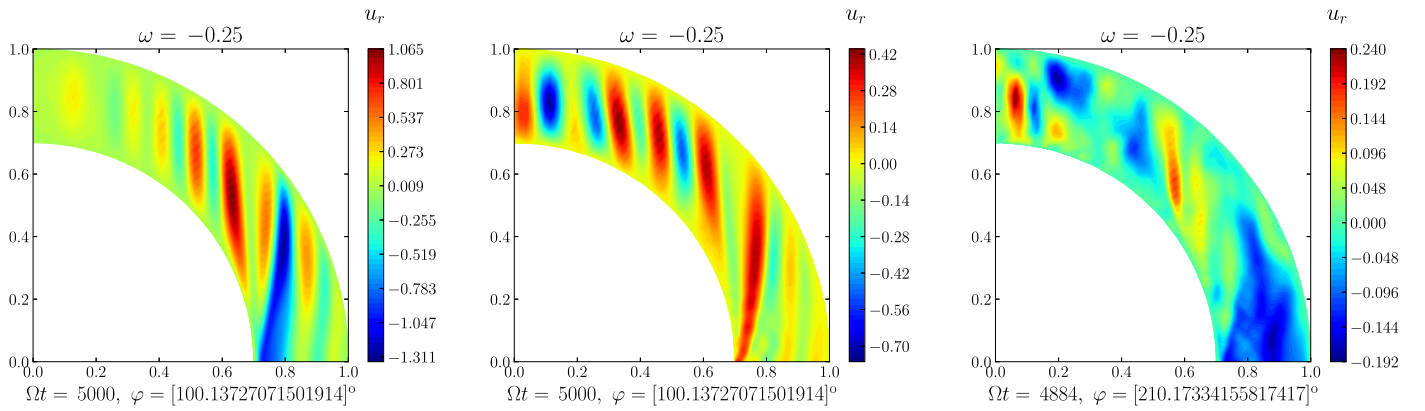


Figure 3. Meridional slice of radial velocity u_r in one quadrant with $\omega = -0.25$ and $\alpha = 0.7$ (and $E = 10^{-5}$). Left: $C_t = 10^{-3}$ (approximately linear). Linear calculations with the spectral code Linear Solver Builder (LSB; Valdetarro et al. 2007) are indistinguishable since nonlinearities are negligible in this case. Middle: $C_t = 10^{-2}$. Right: $C_t = 5 \cdot 10^{-2}$. Note the paradoxical decrease in u_r when increasing C_t .

during the pre-main sequence, probably the dominant phase for IW tidal dissipation (e.g., Barker 2022).

For forcing amplitude $C_t = 10^{-2}$, we find tidal dissipation rates in nonlinear simulations to exhibit very small departures from linear predictions when scanning the full frequency range (not shown; probably due to weak differential rotations with $E_{dr} \lesssim 10^{-6}$). We display in Figure 1(a) the rescaled dissipative quantities $\epsilon_t^{-2} \text{Im}[k_2^2(\omega)]$ and $\epsilon_t^2 Q'_\omega$ and their associated frequency-averaged values for a higher tidal amplitude $C_t = 5 \cdot 10^{-2}$, spanning the full range of frequencies for IWs. The frequency-dependent (reddish bullets indicate final steady-state values) and averaged (purple dotted line) nonlinear tidal dissipation rates do not depart significantly from linear predictions in black (solid and dashed lines, respectively). This is likely to result from the moderate zonal flow strengths triggered, as quantified by $E_{dr} \lesssim 6.2 \cdot 10^{-4}$. The differences are strongest close to “resonant peaks” where dissipation D_ν is maximized (note that division by ω in Λ enhances contributions from small ω), where zonal flows are strongest (see also AB22). The discrepancy between linear and nonlinear frequency-averaged values is approximately 10% here.

Now turning to thicker envelopes with $\alpha = 0.5$, relevant for M stars with masses $\sim 0.4 M_\odot$, or for giant planets with extended dilute strongly stably stratified fluid cores ($\alpha \sim 0.6$ is inferred for Saturn; Mankovich & Fuller 2021)—we find a similar order of magnitude for the discrepancy between linear predictions and nonlinear simulations with $C_t = 10^{-2}$ to those with $\alpha = 0.3$ and $C_t = 5 \cdot 10^{-2}$. For strong tidal forcing with $C_t = 5 \cdot 10^{-2}$, zonal flows are stronger as we can see from the larger values of E_{dr} in Figure 1(b). The frequency-dependent dissipation now departs strongly from the linear prediction by several orders of magnitude for certain frequencies, especially between -1.8 and -0.9 , and between 0.7 and 1.5 , near to the resonant peaks in D_ν . However, the resulting frequency-averaged value deviates by less than 30% from the linear prediction.

In Figure 2, we show results for a solar-like envelope ($\alpha = 0.7$), for both weak $C_t = 10^{-2}$ (panel 2(a)) and strong $C_t = 5 \cdot 10^{-2}$ (panels 2(c) and (d)) forcing, and also for a larger viscosity $E = 5 \cdot 10^{-5}$ (panel 2(b)). We now observe a larger tidal amplitude ($C_t = 5 \cdot 10^{-2}$) or lower viscosity ($E = 10^{-5}$) leads to stronger departures from linear predictions, by up to 3 orders of magnitude at certain frequencies. This is again especially apparent in midrange negative and positive frequencies (and around $\omega = -0.2$, probably associated with the

excitation of a global Rossby mode, seen more clearly for $\alpha = 0.9$). We also observe strong nonlinear effects have flattened the “peaky spectrum” predicted by linear theory by smoothing resonant peaks of enhanced dissipation. This is evidenced more clearly in Figure 2(d), showing the evolution of D_ν versus Doppler-shifted frequency ω/Ω^* (indicating E_{dr} by the colors), following each simulation from its static initial state toward an averaged steady state (corresponding to Figure 2(c)). This shows a strong correlation between E_{dr} , the evolution of D_ν (that departs further from linear predictions when zonal flows are strong), and ω/Ω^* . E_{dr} can be as large as 0.1, indicating very strong tidally driven differential rotation that may be comparable with or even larger than convectively driven differential rotation for large C_t .

It is difficult to predict at a given frequency whether the frequency-dependent dissipation will be attenuated or amplified over linear predictions. The emergence of zonal flows can mitigate the strong activation of intense shear layers, which are associated with the most dissipative peaks, as we observe when comparing the three meridional slices of the radial velocity in Figure 3 at $\omega = -0.25$ (at the peak of linear dissipation for $\alpha = 0.7$). The radial velocity amplitude in the waves *decreases* here as C_t is increased. It is not clear whether hidden global modes (also associated with enhanced dissipation in linear theory; Lin & Ogilvie 2021), still exist in the presence of strong differential rotation. On the other hand, we identify the presence of corotation resonances, for which the Doppler-shifted frequency $\omega - m\delta\Omega$ vanishes (e.g., Astoul et al. 2021), which appear when zonal flows are strong for $C_t = 5 \cdot 10^{-2}$, particularly in the right panel of Figure 3. We emphasize that the frequency and azimuthal wavenumber in this relationship could differ from the (initial) tidal forcing frequency and $m = 2$, since nonlinearities (parametric instabilities or triadic resonances) can excite other modes, such as $m = 1$ with lower frequencies, as seen in AB22 (see also Barik et al. 2018), which could have their own corotation resonances (reminiscent of Weinberg et al. 2012, for gravity waves).

The wave response is very sensitive to α and the initial frequency ω , which dictates both the critical latitude and the angle of IW propagation (hence that of reflection from boundaries). When wave attractors form featuring cyclic behavior with uniform rotation, energy is strongly focused along these, and IWs can be considered to form modes that vary strongly with ω . With corotation resonances, the precise wave frequency, shell thickness, and boundary conditions may

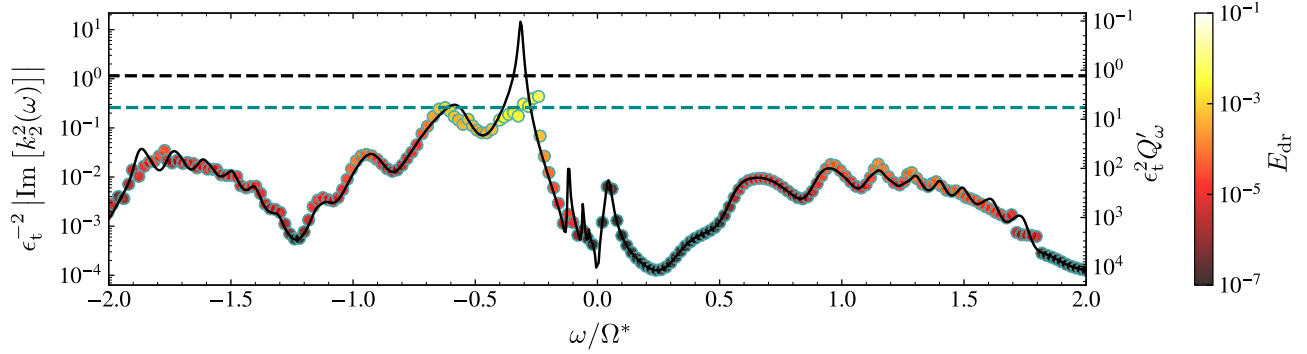


Figure 4. The same as Figure 1 but for $\alpha = 0.9$ and $C_t = 10^{-2}$. E_{dr} is maximal when $\omega = -0.26$ with $E_{dr} = 7.8 \cdot 10^{-3}$ and minimal when $\omega = 0.26$ with $E_{dr} = 4.3 \cdot 10^{-10}$.

matter less, since waves probably travel from critical latitudes where they are launched until they reach a corotation resonance where they are mostly damped (e.g., Astoul et al. 2021) without being able to form “global modes.” In this “traveling wave” regime (like that for gravity waves approaching critical layers; e.g., Zahn 1975; Goodman & Dickson 1998; Barker & Ogilvie 2010), we might hypothesize that the dissipation may only depend on the efficiency with which waves are excited, rather than on the precise dissipative mechanism or shape of the container. If so, this might explain the “flattening” of the dissipation observed in Figure 2(d) when nonlinear effects and E_{dr} are strong. This hypothesis is supported by observing corotation resonances for other initial frequencies than $\omega = -0.25$.

Nonlinear effects also mitigate the frequency-averaged tidal dissipation compared with linear predictions, as we observe in Figures 1 and 2. The strongest reduction is approximately a factor of 3 for $C_t = 5 \cdot 10^{-2}$ and $E = 10^{-5}$ (Figure 2(c)). For $\alpha = 0.9$ (see Figure 4), appropriate for F-stars or giant planets outside their dynamo regions⁶, and $C_t = 10^{-2}$, the nonlinear frequency-averaged dissipation is reduced even further from linear predictions (by a factor of 4). This mainly results from the dominant peak of linear dissipation at $\omega = -1/3$ (corresponding to Rossby mode excitation; Ogilvie 2009) being significantly reduced by differential rotation, while for other frequencies with weaker zonal flows, nonlinear results mostly follow their linear predictions. We would expect an even larger reduction in the frequency-averaged dissipation for $C_t = 5 \cdot 10^{-2}$ (which are even more demanding cases to resolve spatially and temporally).

4. Application to Star–Planet and Binary Star Systems

4.1. Star–Planet Systems

Tidal interactions drive two-body systems toward a stable equilibrium with circular and (equatorially) coplanar orbits, and both rotation periods synchronized with the orbital period (with sufficient angular momentum, otherwise orbital decay toward coalescence is predicted; Hut 1980). Many close-in planets observed are likely to be synchronized and (mostly) circularised because of strong tidal dissipation in these planets, probably due to IWs (e.g., Ogilvie & Lin 2004; Wu 2005; Goodman & Lackner 2009; Barker 2016). Synchronization of stellar rotation usually operates on much longer timescales.

⁶ The upper differentially rotating convective zones of Jupiter and Saturn where zonal flows extend above fractional radii of ~ 0.96 and ~ 0.86 , respectively (see, e.g., Guillot et al. 2022).

Damping of IWs in convective envelopes of planet-hosting stars is a possible avenue for tidal dissipation if stars rotate sufficiently rapidly to permit their excitation (requiring $|\omega| \leq 2\Omega$). Two such examples may be WASP-128 and KELT-1 (Hodžić et al. 2018; Maciejewski et al. 2022), both composed of massive brown dwarfs ($37 M_J$ and $27 M_J$, respectively) orbiting in $P_o = 2.21$ and $P_o = 1.22$ days around main-sequence stars (of masses $1.16 M_\odot$ and $1.34 M_\odot$) with rotation periods $P_* \approx 2.93$ and $P_* \approx 1.52$ days (using von Essen et al. 2021, for KELT-1), respectively. IWs can be tidally excited in the stellar envelopes since their (asynchronous) tidal frequencies $\omega/\Omega_* = 2(P_*/P_o - 1)$ are, respectively, $\omega/\Omega_* \approx 0.65$ and $\omega/\Omega_* \approx 0.5$ (so $|\omega| \leq 2\Omega_*$). Once these stars become synchronized with their orbits, the companion may subsequently decay on the magnetic braking timescale (e.g., Barker & Ogilvie 2009; Damiani & Lanza 2015).

The stellar tidal amplitudes in WASP-128 and KELT-1 are $\epsilon_* \approx 10^{-4}$ and $\epsilon_* \approx 4 \cdot 10^{-4}$, respectively, two of the highest⁷ in stars hosting planetary companions. For $C_t \ll 10^{-2}$ with $E \gtrsim 10^{-5}$ (as predicted for turbulent viscosities by mixing-length theory or simulations; e.g., Bekki et al. 2022), we have shown that nonlinear effects may not significantly modify tidal dissipation in our model (though this statement may not hold for lower viscosities, such as if microscopic rather than turbulent viscosities are relevant for E). We can nevertheless derive both the linear frequency-dependent and averaged modified tidal quality factors for these systems. We predict $Q'_\omega \approx 7 \cdot 10^4$ for WASP-128 and $Q'_\omega \approx 8 \cdot 10^4$ for KELT-1 using the frequencies above with $\alpha = 0.9$ (black solid curve in Figure 4) and Equation (8) with $\epsilon_\Omega \approx 0.046$ and $\epsilon_\Omega \approx 0.12$, respectively, in our homogeneous stellar model. The lower bound for KELT-1 b is constrained from observations to be $Q' \approx 2.33^{+0.36}_{-0.38} \cdot 10^6$ given that orbital evolution has not been unambiguously detected (as for WASP-128 b). The prediction for frequency-averaged IW tidal dissipation is $Q' \approx 2.6 \cdot 10^6$ for KELT-1 (Barker 2020; Maciejewski et al. 2022), based on a realistic fluid model,⁸ and Hodžić et al. (2018) inferred $Q' \approx 10^7$ for WASP-128 assuming a dynamical equilibrium where tidal and wind braking torques balance. Thus, the

⁷ We expect $C_t \approx \epsilon_*$ since $k_2 \ll 1$ given the thin envelopes of main-sequence G and F stars (though k_2 could be larger and $O(1)$ during the pre-main sequence).

⁸ Our model predicts frequency-averaged values (Equation (10)) $Q' \approx 6 \cdot 10^2$ for KELT-1 and $Q' \approx 90$ for WASP-128. However, assuming a homogeneous body with a dense core may be less applicable for thin shells ($\alpha = 0.9$) due to the strong resonant peak at $\omega \approx -1/3$. Discrepancies with more realistic models are highest for such large α (e.g., Figure –7 of Ogilvie 2013).

Table 1Tidal Quality Factors Q'_ω (Frequency-dependent) and Q' (Frequency-averaged) for Eccentricity Tides in Hot Jupiters

α	Q'_ω (l)	Q'_ω (nl)	Q' (l)	Q' (nl)
0.3	10^5	$[10^5, 2 \cdot 10^5]$	$5 \cdot 10^4$	$[5 \cdot 10^4, 5 \cdot 10^4]$
0.5	$7 \cdot 10^4$	$[7 \cdot 10^4, 8 \cdot 10^4]$	$3 \cdot 10^3$	$[4 \cdot 10^3, 5 \cdot 10^3]$
0.7	$3 \cdot 10^3$	$[3 \cdot 10^3, 10^4]$	$6 \cdot 10^2$	$[8 \cdot 10^2, 10^3]$
0.9	$8 \cdot 10^3$	$7 \cdot 10^3$	$8 \cdot 10^1$	$3 \cdot 10^2$

Note. We compute linear (l) and nonlinear (nl) estimates assuming $k_2 = 0.3$ and $\epsilon_\Omega = 0.1$. Values in brackets are for $C_t = [10^{-2}, 5 \cdot 10^{-2}]$ (otherwise $C_t = 10^{-2}$).

operation of IW dissipation is not inconsistent with these observations.

The tidal amplitude inside planets ϵ_p is typically much larger than ϵ_* (Figure 23 of AB22). However, planetary rotation rates Ω_p are unknown, and usually assumed to be synchronized, i.e., $\Omega_p \approx \Omega_o$ (probably driven by IW dissipation). We have more information on planetary eccentricities e , and we can make predictions for when eccentricity tides (i.e., when $e \neq 0$ drives tidal interactions, for which tidal amplitudes are $\propto e$) may become nonlinear. The frequency for a given (n, m) tidal component is $\omega = n\Omega_o - m\Omega_p$, where n labels temporal harmonics of the orbital motion, and $(m, n) = (2, 3)$ is usually dominant (but $(m, n) \in \{(2, 1), (0, 1)\}$ can also contribute; Ogilvie 2014). Assuming $\Omega_p = \Omega_o$, we have $\omega/\Omega_p = 1$ (-1 with $n = 1$). We have searched the exoplanet.eu database for planets satisfying $7e C_t/2 > 10^{-2}$, assuming $k_2 = 0.3$ as a lower bound⁹ (see also Dewberry & Lai 2022 for k_2 computations in fast rotators), which selects HAT-P-65 b, HAT-P-67 b, HATS-18 b, and HATS-24 b. These are inflated planets (see Jupiter and $e \gtrsim 0.1$), which rotate at approximately 10% of their breakup velocities (assuming synchronism, i.e., $\epsilon_\Omega \approx 0.1$) and tidal amplitudes $7e C_t/2$ as large as 10^{-2} for HATS-24 b, HATS-18 b, HAT-P-67 b, and closer to $5 \cdot 10^{-2}$ for HAT-P-65 b. Nonlinear IW effects are likely to be even more important (with larger C_t) for the past tidal evolution of Hot Jupiter systems since young planets have larger radii, probably rotate more rapidly, and may not have been tidally synchronized or circularized. Table 1 provides both the linear and nonlinear predictions for Q' (frequency-dependent and averaged) for these systems, for various α as planetary internal structures are uncertain. Varying α leads to important numerical differences in Q' , which span the range from 10^2 to 10^5 , with even higher values for a tiny core ($Q' > 10^7$ for $\alpha = 0.1$). However, the linear and nonlinear frequency-dependent estimates are often comparable, with moderate discrepancies when $C_t = 5 \cdot 10^{-2}$. The frequency-averaged Q' is generally smaller than the frequency-dependent value, except close to resonant peaks. This is because the former is dominated by resonant peaks in linear theory. The strong dependence on α suggests the possibility of constraining planetary structures from observations inferring their tidal evolution.

⁹ Based on constraints for the Hot Jupiters HAT-P-13 b ($k_2 = 0.31^{+0.08}_{-0.05}$; Buhler et al. 2016), WASP-121 b ($k_2 = 0.39 \pm 0.8$; Hellard et al. 2019), and WASP-103 b ($k_2 = 0.59^{+0.45}_{-0.53}$; Barros et al. 2022).

4.2. Application to Late-type Eclipsing Binaries

There is strong evidence for tidal circularization and synchronization in late-type binaries (e.g., Meibom & Mathieu 2005; Meibom et al. 2006). Equilibrium tides are not believed to be sufficient to explain the circularization of old binaries¹⁰ (Zahn & Bouchet 1989; Mathieu et al. 2004; Zahn 2013), but the dissipation of IWs could explain observations (Barker 2022). Regarding tidal synchronization, Lurie et al. (2017) reported rotation periods for several hundred low-mass stars in eclipsing binaries (EBs). The majority are approximately synchronized, but a substantial fraction rotate subsynchronously, possibly because they feature differential rotation or because synchronization is ongoing. We calculate Q' for the asynchronous tide in these systems due to IW dissipation in their convective envelopes. We choose EBs satisfying $P_o > P_1/2$ (for IW excitation), where P_1 is the primary's rotation period (i.e., the more massive star, using $P_{1 \min}$ in Table 2 of Lurie et al. 2017; Patel & Penev 2022). To compute ϵ and ϵ_Ω , we also use data in Windemuth et al. (2019; i.e., masses, radii, and ages). We enforce $\epsilon > 10^{-2}$, inferring a using Kepler's third law, and list the selected Kepler EBs in Table 2. M_1 is rounded to the nearest tenth to match stellar models (computed with STAREVOL; Amard et al. 2019; Astoul et al. 2019) to infer both α (rounded to the nearest value in Section 3) and $k_2 = 3\rho/(5\bar{\rho} - 3\rho)$ (see Ogilvie 2013 for a similar homogeneous fluid model) at a given age, with $\bar{\rho}$ the mean stellar density and ρ the density in the middle of the envelope. The (non)linear Q'_ω is computed using Equation (8) with $\omega/\Omega = 2(P_1/P_o - 1)$, taken from our closest model (α, C_t). The (non)linear frequency-averaged $Q' = 3/(2\Delta)$ is computed using Equation (10) (Equation (9)). We notice significant discrepancies, sometimes by several orders of magnitude (e.g., the first system), between frequency-dependent and frequency-averaged values. The moderate C_t in these systems prevents nonlinear effects from significantly impacting quality factors (for the E studied). The dissipation is very heterogeneous depending on the system, with $1.7 < \log_{10} Q'_\omega < 6$, typically much lower than the frequency-averaged predictions in Barker (2022, Figure 1), where $Q' \approx 10^7 (P_1/10 \text{ d})^2$ for main-sequence $0.2\text{--}1.2 M_\odot$ stars. This difference is partly related to the density variation throughout the body allowed in Barker (2022), and the adoption of a rigid core here, both of which are important assumptions to relax in future simulations.

5. Conclusions

We have simulated tidally forced inertial waves in hydrodynamical spherical shell models of convective envelopes in rotating low-mass stars and giant planets. Our main goal was to determine the validity of linear theory, and particularly the widely applied frequency-averaged inertial wave dissipation, in modeling tidal dissipation in stars and planets.

Our nonlinear simulations have demonstrated that the strongly frequency-dependent dissipation predicted by linear theory is increasingly smoothed out by nonlinearities for increasing tidal amplitudes (larger C_t), for thinner shells (larger α), and for smaller viscosities (smaller E). Our results predict tidal energy transfer rates that differ from linear predictions by up to 3 orders of magnitude at a given frequency due to the generation of differential rotation and its back-reaction on the

¹⁰ See Terquem (2021) for arguments to the contrary.

Table 2
Frequency-dependent and Averaged Modified Tidal Quality Factors Q'_ω and Q' from Linear (l) and Nonlinear (nl) Simulations for Several EBs

System (KIC)	ϵ ($\times 10^{-2}$)	M_1	age	α	ω	k_2	ϵ_Ω	Q'_ω (l)	Q'_ω (nl)	Q' (l)	Q' (nl)	Q_A'
10257903	1.7	1	$7.1 \cdot 10^9$	0.7	0.27	$2 \cdot 10^{-2}$	0.18	10^6	10^6	$3 \cdot 10^2$	$4 \cdot 10^2$	10^5
9020426	1.3	1	$7.8 \cdot 10^6$	0.5	-0.3	0.4	0.19	$6 \cdot 10^3$	$7 \cdot 10^3$	$8 \cdot 10^2$	10^3	$6 \cdot 10^3$
8155368	2.4	0.8	10^{10}	0.7	-0.94	0.2	0.46	$5 \cdot 10^1$	$[5 \cdot 10^1, 2 \cdot 10^2]$	$3 \cdot 10^1$	$[5 \cdot 10^1, 8 \cdot 10^1]$	10^4
7985167	1.5	1.3	$3.5 \cdot 10^9$	0.9	-0.72	10^{-3}	0.28	$3 \cdot 10^2$	$2 \cdot 10^2$	$2 \cdot 10^1$	$7 \cdot 10^1$	$8 \cdot 10^4$
7885570	1.7	1.5	$2.3 \cdot 10^9$	0.9	-0.52	$2 \cdot 10^{-4}$	0.29	10^2	$2 \cdot 10^2$	$2 \cdot 10^1$	$7 \cdot 10^1$	$2 \cdot 10^5$
6311637	1.4	1.4	$3.5 \cdot 10^9$	0.9	-0.66	$3 \cdot 10^{-4}$	0.30	10^2	$7 \cdot 10^1$	10^1	$7 \cdot 10^1$	10^5
6283224	1.2	1	$5.3 \cdot 10^9$	0.7	-1.24	10^{-2}	0.42	$6 \cdot 10^4$	$6 \cdot 10^4$	$5 \cdot 10^1$	$8 \cdot 10^1$	$9 \cdot 10^3$
3662635	1.2	1.3	$5.6 \cdot 10^8$	0.9	0.04	$2 \cdot 10^{-4}$	0.15	10^4	10^4	$6 \cdot 10^1$	$3 \cdot 10^2$	10^6
3344427	1.3	0.9	$6.7 \cdot 10^9$	0.7	-0.77	$3 \cdot 10^{-2}$	0.27	$6 \cdot 10^3$	$6 \cdot 10^3$	10^2	$2 \cdot 10^2$	$2 \cdot 10^4$
2447893	1.5	0.9	$1.4 \cdot 10^7$	0.5	0.21	0.3	0.16	$3 \cdot 10^5$	$8 \cdot 10^5$	10^3	$2 \cdot 10^3$	$5 \cdot 10^4$

Note. Nonlinear values in brackets are for $C_t = [10^{-2}, 5 \cdot 10^{-2}]$ (otherwise $C_t = 10^{-2}$). The last column shows approximate frequency-averaged linear predictions from Barker (2022) accounting for realistic stellar density profiles: $Q_A' \approx 10^7(P_1/10 \text{ d})^2$ for main-sequence $0.2\text{--}1.2M_\odot$ stars or their Figure 1 (top panel). This can differ substantially from our predictions for the frequency-averaged value in particular (less so for Q'_ω).

waves. However, we have found the frequency-averaged prediction from linear theory to be more robust, typically predicting the frequency-averaged nonlinear dissipation to within a factor of 4. The largest disagreements are found where nonlinearities are strongest, and the strongest peaks of linear dissipation are substantially attenuated.

This suggests that the frequency-averaged linear theory predictions for inertial wave dissipation are relatively robust even when including nonlinear effects, and thus may be reasonable to apply to modeling tidal evolution of stellar and planetary statistical populations. However, we caution that tidal evolution in a given system (at a given time and tidal frequency) might differ substantially. It may also greatly change when taking into account realistic density profiles, especially for thin shells, and the influence of a radiative interior—here modeled as a rigid core, so assumed to be strongly stratified as expected in low-mass stars. Otherwise, when the buoyancy frequency at the radiative/convective interface is comparable to rotation (as expected for Jupiter and Saturn; e.g., Mankovich & Fuller 2021), tidal dissipation from inertial waves could be mitigated by the presence of a stably stratified dilute core (for Jupiter, Dewberry 2023; Lin 2023, Dhoubi et al. submitted) or on the contrary enhanced (for Saturn, Pontin et al. submitted). Future work should explore the sensitivity of boundary conditions and more realistic planetary/stellar structures on (non)linear simulations and how well using the frequency-averaged value models tidal evolution in real frequency-dependent systems.

The “smoothing-out” of the dissipation predicted by linear theory is reminiscent of the transition from global modes (with strongly frequency-dependent dissipation) to traveling waves (with much weaker dependence on frequency) for tidally excited gravity waves in stellar radiation zones. We have identified the key role of corotation resonances (where the Doppler-shifted wave frequency vanishes) that may explain this tendency in our simulations of tidally generated differential rotation. It is essential to explore further the role of turbulent convection and convectively generated differential rotation. Tidal generation of differential rotation may compete with convection in the closest binaries or in Hot Jupiters. Our work thus motivates further studies of tidal inertial waves and of their interactions with differential rotation, turbulent convection, and magnetic fields using more realistic density profiles. Finally, it

would be worth exploring models permitting realistic nonlinear couplings between wavelike and nonwavelike tidal flows.

Acknowledgments

Funded by STFC grants ST/S000275/1 and ST/W000873/1, and by a Leverhulme Trust Early Career Fellowship to A.A. Simulations were undertaken on the DiRAC Data Intensive service at Leicester, operated by the University of Leicester IT Services, which forms part of the STFC DiRAC HPC Facility (www.dirac.ac.uk). The equipment was funded by BEIS capital funding via STFC capital grants ST/K000373/1 and ST/R002363/1 and STFC DiRAC Operations grant ST/R001014/1. DiRAC is part of the National e-Infrastructure. This research has made use of data obtained from or tools provided by the portal exoplanet.eu of The Extrasolar Planets Encyclopaedia, and of NASA’s Astrophysics Data System Bibliographic Services. We thank M. Rieutord, R. V. Valdetaro, and C. Baruteau for providing the LSB code, and S. Mathis, A. Guseva and the referee for helpful comments.

Facilities: CDS, ADS.

Software: MagIC dynamo code (version 5.10) at <https://magic-sph.github.io/>, STAREVOL (Amard et al. 2019), LSB (Rieutord & Valdetaro 2010).

Appendix A

Discussion on Tidally Induced Zonal Flows

A.1. Tidal Forcing Amplitude Dependence

The structures of the zonal flows generated by IW nonlinear interactions are difficult to predict as they are strongly dependent on the initial tidal frequency, core size, and Ekman number, which dictate the shear layer structure and the locations of strong dissipation inside the shell. Though the energy inside the differential rotation typically increases with decreasing Ekman number, the nature of this dependence varies with frequency in a nontrivial way (see Figure 22 of Astoul & Barker 2022). In Figures 5 and 6, we explore the zonal flow strength’s dependence on tidal amplitude for a fixed tidal frequency, core size, and Ekman number. Curiously, two regimes clearly emerge depending on the strength of nonlinear effects. In the weakly nonlinear regime for $C_t \lesssim 10^{-3}$, we can anticipate this regime following Tilgner (2007) and Astoul & Barker (2022). Using the notations u_1 for the linear tidal flow

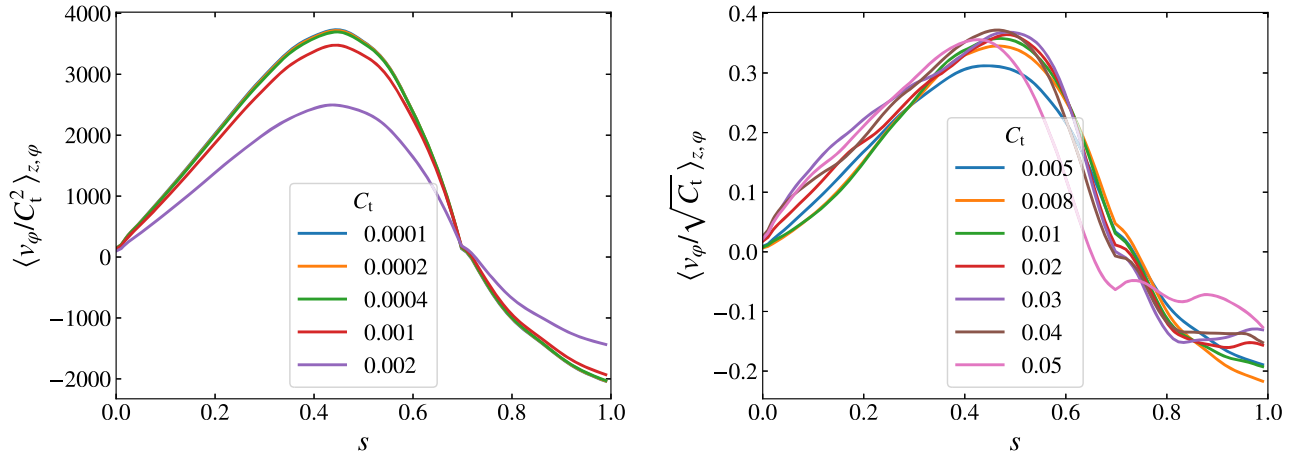


Figure 5. Azimuthal and vertical average of the azimuthal velocity normalized by the tidal amplitude squared $\langle v_\phi / C_t^2 \rangle_{z,\phi}$ (left), or by $\langle v_\phi / \sqrt{C_t} \rangle_{z,\phi}$ (right), against the distance to the rotation axis s , for low (left) and moderate to high (right) values of the tidal amplitude C_t in different colors. The tidal frequency, core size, and Ekman number are set to $\omega = -0.25$, $\alpha = 0.7$, and $E = 10^{-5}$, respectively, in both panels.

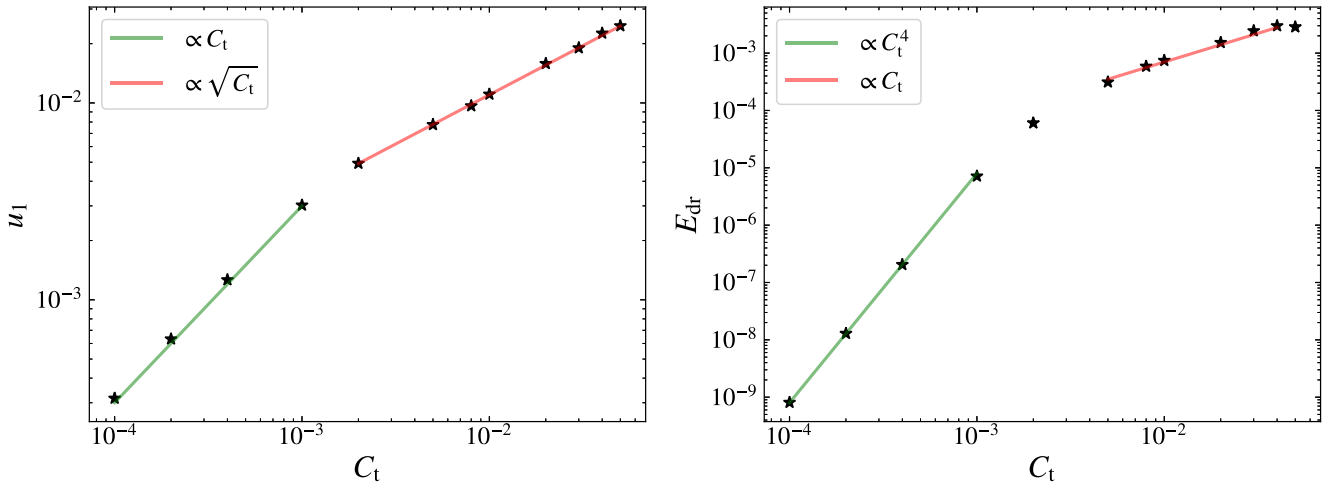


Figure 6. Left: nonaxisymmetric component of the tidal flow magnitude u_1 against the tidal amplitude C_t , when filtering out the zonal flow $m = 0$ component from the kinetic energy spectrum summed over $m \neq 0$ components. Right: energy in the differential rotation E_{dr} against tidal amplitude C_t . The different nonlinear regimes are indicated with colored lines in both panels. The tidal frequency, core size, and Ekman number are set to $\omega = -0.25$, $\alpha = 0.7$, and $E = 10^{-5}$, respectively.

and u_2 for the induced zonal flow, the scaling law $u_2 \propto u_1^2 \propto C_t^2$ is directly obtained from balancing zonal flow viscous dissipation $E\Delta u_2$ with the nonlinear advection term $(\mathbf{u}_1 \cdot \nabla)u_1$, which forces the zonal flow. This regime is evidenced for $C_t \lesssim 10^{-3}$ in Figure 5 for the zonal flow profile, and in Figure 6 (green scaling), where we show that $u_1 \propto C_t$ (time derivative and/or the Coriolis force acting on u_1 balances tidal forcing) and $E_{dr} \propto u_2^2 \propto C_t^4$. Note that both the zonal flow and tidal inertial wave length scales are independent of C_t (as shown in Figure 5 for the zonal flow). In the moderately nonlinear regime for $2 \cdot 10^{-3} \lesssim C_t < 5 \cdot 10^{-2}$, u_1 is proportional to $\sqrt{C_t}$ (as is u_2), as we show in Figure 5 (right panel) and Figure 6 (left panel, red scaling), making $E_{dr} \propto u_2^2 \propto C_t$ (right panel, red scaling). Such a scaling can be obtained if the waves satisfy a balance between nonlinear advection $(\mathbf{u}_1 \cdot \nabla)u_1$ and tidal forcing, and then if the axisymmetric component of $(\mathbf{u}_1 \cdot \nabla)u_1$ balances $(\mathbf{u}_2 \cdot \nabla)u_2$. For the strongly nonlinear regime when $C_t \geq 5 \cdot 10^{-2}$, E_{dr} seems to saturate (right panel of Figure 6), possibly because hydrodynamical instabilities limit zonal flow strengths to become independent of the tidal forcing amplitude.

A.2. Time to Generate Zonal Flows

For all simulations, we assume their typical timescales are fast compared with tidal evolutionary timescales so that we can treat the equilibrium with a prescribed (not secularly evolving) time-dependent flow. Given that resonant peaks of tidal dissipation may induce fast changes in the dynamical evolution of orbits and rotations and hence the tidal frequency, unless coincident changes in internal structure or rotation evolve to maintain resonances (e.g., Witte & Savonije 2002; Fuller et al. 2016; Lainey et al. 2020), one can wonder if the development of zonal flows at a peculiar resonant tidal frequency (i.e., for a specific configuration of the system) are fast enough compared to tidal evolution timescales for our results regarding them to be valid. In our simulations, we observe that the energy in the differential rotation reaches a steady state after a few thousand Ω^{-1} units (as shown in Figure 7, and also in Astoul & Barker 2022). Indeed, for low amplitudes, a saturated state is reached when the rate of local angular momentum deposition into the mean flow by the waves balances the (presumably turbulent in reality) viscous damping rate for the mean flow. This rate is also dependent on C_t , and proportional to u_1^2 , so the zonal flow is faster to develop for

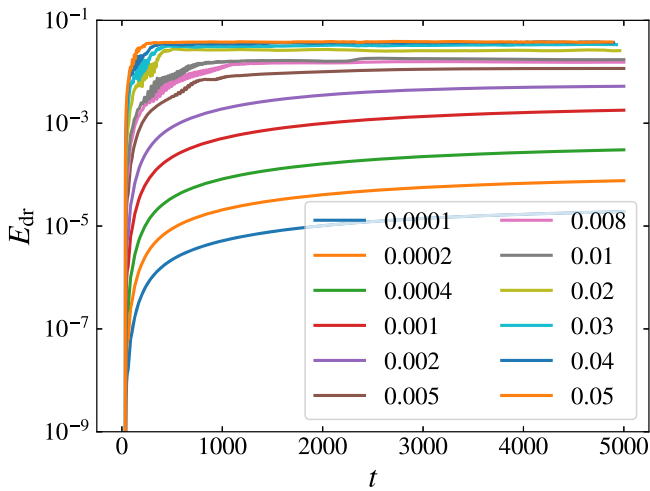


Figure 7. Energy in the differential rotation E_{dr} against time for different tidal forcing amplitudes C_t shown in different colors. The tidal frequency, core size, and Ekman number are set to $\omega = -0.25$, $\alpha = 0.7$, and $E = 10^{-5}$, respectively.

higher tidal amplitude forcing (see Appendix A.1 and Figure 7). When estimating the zonal flow length scale to be a few tenths of the radius of the body, for instance, $l/R \sim 0.2$ (e.g., Figure 5), the corresponding viscous timescale is $\tau_\nu = l^2/Ek \sim 4000\Omega^{-1}$ for $E = 10^{-5}$ (even shorter for high C_t as evidenced in Figure 7). For a fast 1 day or 10 day rotating young star, this means timescales of approximately 10–100 yr. This time is short, and probably shorter than tidal evolutionary timescales. As a result, it is plausible that tidally induced differential rotation has enough time to set in before the system evolves out of the resonance—and more globally for every tidal frequency not in a resonant peak. We stress that this statement may only be valid when using mixing-length theory (large) estimates for the viscosity. (On the other hand, if we apply tiny values of atomic viscosity involving $E = 10^{-12}$ or lower, viscous forces may be too weak for such a balance to be attained before the system has evolved through a resonant peak). To conclude, we find that tidal generation of zonal flows can be very rapid for large C_t (even a few hundred rotation times for large C_t , since the angular momentum deposition is faster, as evidenced in Figure 7), and due to the localized nature of the differential rotation produced, this can happen prior to changing the bulk rotation of the body (see the related problem of gravity waves in stars, e.g., Guo et al. 2023).

ORCID iDs

Aurélien Astoul  <https://orcid.org/0000-0002-8561-0769>
 Adrian J. Barker  <https://orcid.org/0000-0003-4397-7332>

References

- Amard, L., Palacios, A., Charbonnel, C., Gallet, F., & Bouvier, J. 2016, *A&A*, **587**, A105
- Amard, L., Palacios, A., Charbonnel, C., Gallet, F., Georgy, C., Lagarde, N., & Siess, L. 2019, *A&A*, **631**, A77
- Astoul, A., & Barker, A. J. 2022, *MNRAS*, **516**, 2913
- Astoul, A., Mathis, S., Baruteau, C., et al. 2019, *A&A*, **631**, A111
- Astoul, A., Park, J., Mathis, S., Baruteau, C., & Gallet, F. 2021, *A&A*, **647**, A144
- Barik, A., Triana, S. A., Hoff, M., & Wicht, J. 2018, *JFM*, **843**, 211
- Barker, A. J. 2016, *MNRAS*, **459**, 939
- Barker, A. J. 2020, *MNRAS*, **498**, 2270
- Barker, A. J. 2022, *ApJL*, **927**, L36
- Barker, A. J., & Astoul, A. A. V. 2021, *MNRAS*, **506**, L69
- Barker, A. J., & Ogilvie, G. I. 2009, *MNRAS*, **395**, 2268
- Barker, A. J., & Ogilvie, G. I. 2010, *MNRAS*, **404**, 1849
- Barros, S. C. C., Akınanmi, B., Boué, G., et al. 2022, *A&A*, **657**, A52
- Baruteau, C., & Rieutord, M. 2013, *JFM*, **719**, 47
- Bekki, Y., Cameron, R. H., & Gizon, L. 2022, *A&A*, **666**, A135
- Bolmont, E., Gallet, F., Mathis, S., et al. 2017, *A&A*, **604**, A113
- Bolmont, E., & Mathis, S. 2016, *CeMDA*, **126**, 275
- Buhler, P. B., Knutson, H. A., Batygin, K., et al. 2016, *ApJ*, **821**, 26
- Damiani, C., & Lanza, A. F. 2015, *A&A*, **574**, A39
- Dewberry, J. W. 2023, *MNRAS*, **521**, 5991
- Dewberry, J. W., & Lai, D. 2022, *ApJ*, **925**, 124
- Duguid, C. D., Barker, A. J., & Jones, C. A. 2020, *MNRAS*, **491**, 923
- Favier, B., Barker, A. J., Baruteau, C., & Ogilvie, G. I. 2014, *MNRAS*, **439**, 845
- Fuller, J., Luan, J., & Quataert, E. 2016, *MNRAS*, **458**, 3867
- Gallet, F., Bolmont, E., Mathis, S., Charbonnel, C., & Amard, L. 2017, *A&A*, **604**, A112
- Goldreich, P. 1963, *MNRAS*, **126**, 257
- Goodman, J., & Dickson, E. S. 1998, *ApJ*, **507**, 938
- Goodman, J., & Lackner, C. 2009, *ApJ*, **696**, 2054
- Guenel, M., Baruteau, C., Mathis, S., & Rieutord, M. 2016, *A&A*, **589**, A22
- Guillot, T., Fletcher, L. N., Helled, R., et al. 2022, arXiv:2205.04100
- Guo, Z., Ogilvie, G. I., & Barker, A. J. 2023, *MNRAS*, **521**, 1353
- Hellard, H., Csizmadia, S., Padovan, S., et al. 2019, *ApJ*, **878**, 119
- Hodžić, V., Triard, A. H. M. J., Anderson, D. R., et al. 2018, *MNRAS*, **481**, 5091
- Hut, P. 1980, *A&A*, **92**, 167
- Lainey, V., Casajus, L. G., Fuller, J., et al. 2020, *NatAs*, **4**, 1053
- Lazovik, Y. A. 2021, *MNRAS*, **508**, 3408
- Lin, Y. 2023, *A&A*, **671**, A37
- Lin, Y., & Ogilvie, G. I. 2018, *MNRAS*, **474**, 1644
- Lin, Y., & Ogilvie, G. I. 2021, *ApJL*, **918**, L21
- Lurie, J. C., Vyhmeister, K., Hawley, S. L., et al. 2017, *AJ*, **154**, 250
- Maciejewski, G., Fernandez, M., Sota, A., et al. 2022, *A&A*, **667**, A127
- Mankovich, C. R., & Fuller, J. 2021, *NatAs*, **5**, 1103
- Mathieu, R. D., Meibom, S., & Dolan, C. J. 2004, *ApJL*, **602**, L121
- Mathis, S. 2015, *A&A*, **580**, L3
- Meibom, S., & Mathieu, R. D. 2005, *ApJ*, **620**, 970
- Meibom, S., Mathieu, R. D., & Stassun, K. G. 2006, *ApJ*, **653**, 621
- Ogilvie, G. I. 2009, *MNRAS*, **396**, 794
- Ogilvie, G. I. 2013, *MNRAS*, **429**, 613
- Ogilvie, G. I. 2014, *ARA&A*, **52**, 171
- Ogilvie, G. I., & Lin, D. N. C. 2004, *ApJ*, **610**, 477
- Ogilvie, G. I., & Lin, D. N. C. 2007, *ApJ*, **661**, 1180
- Patel, R., & Penev, K. 2022, *MNRAS*, **512**, 3651
- Rieutord, M., & Valdetarro, L. 2010, *JFM*, **643**, 363
- Terquem, C. 2021, *MNRAS*, **503**, 5789
- Tilgner, A. 2007, *PhRvL*, **99**, 194501
- Valdetarro, L., Rieutord, M., Braconnier, T., & Fraysse, V. 2007, *JCoAM*, **205**, 382
- Vidal, J., & Barker, A. J. 2020a, *ApJL*, **888**, L31
- Vidal, J., & Barker, A. J. 2020b, *MNRAS*, **497**, 4472
- von Essen, C., Mallonn, M., Piette, A., et al. 2021, *A&A*, **648**, A71
- Wei, X. 2018, *ApJ*, **854**, 34
- Weinberg, N. N., Arras, P., Quataert, E., & Burkart, J. 2012, *ApJ*, **751**, 136
- Windemuth, D., Agol, E., Ali, A., & Kiefer, F. 2019, *MNRAS*, **489**, 1644
- Witte, M. G., & Savonije, G. J. 2002, *A&A*, **386**, 222
- Wu, Y. 2005, *ApJ*, **635**, 688
- Zahn, J. P. 1975, *A&A*, **41**, 329
- Zahn, J.-P. 2013, in *Stellar Tides*, ed. J. Souchay, S. Mathis, & T. Tokieda, Vol. 861 (Heidelberg: Springer), 301
- Zahn, J. P., & Bouchet, L. 1989, *A&A*, **223**, 112